Key Points:

- We identify high sub-mesoscale sea surface slope (SSS) variability over western boundary currents and regions of rough topography
- Seasonal variations are small (<10% in amplitude) compared to the mean variability on length scales from 30 to 100 km
- SSS variation is related to the significant wave height and thermocline depth

Supporting Information:

Supporting Information may be found in the online version of this article.

Author Contributions:

Conceptualization: Y. Yu, D. T. Sandwell, S. T. Gille
Formal analysis: Y. Yu, D. T. Sandwell, S. T. Gille
Funding acquisition: D. T. Sandwell
Investigation: Y. Yu, D. T. Sandwell, S. T. Gille
Methodology: Y. Yu, D. T. Sandwell, S. T. Gille
Project Administration: D. T. Sandwell
Resources: D. T. Sandwell, S. T. Gille
Software: Y. Yu, D. T. Sandwell
Supervision: D. T. Sandwell, S. T. Gille
Validation: Y. Yu, D. T. Sandwell, S. T. Gille
Visualization: Y. Yu, D. T. Sandwell
Writing – original draft: Y. Yu, D. T. Sandwell, S. T. Gille
Writing – review & editing: Y. Yu, D. T. Sandwell, S. T. Gille

Seasonality of the Sub-Mesoscale to Mesoscale Sea Surface Variability From Multi-Year Satellite Altimetry

Y. Yu[1] [ID]**, D. T. Sandwell[1]** [ID]**, and S. T. Gille[1]** [ID]

[1]Scripps Institution of Oceanography, University of California, San Diego, La Jolla, CA, USA

Abstract Sea surface slope (SSS) varies in response to a range of physical processes: tides, geostrophic flows, surface and internal waves, etc. We present the sea surface variation in the form of the SSS variability using 30 years of heterogeneous satellite altimetry measurements. We apply band-pass filters to the along-track SSS, and derive the mean and seasonal (annual and semi-annual) components of SSS variability in multiple wavelength sub-bands from 10 to 1,000 km. We show that the seasonal components are generally small (<10% in amplitude) compared to the mean variability. Through correlation analysis, we show evidence that SSS variability with wavelengths less than 30 km is dominated by wave height noise. At sub-mesoscale to mesoscale (30–100 km) wavelengths, we identify high variability over western boundary currents and regions of rough topography. In this band, the high-latitude Northern Hemisphere and the south Indian Ocean are associated with large annual cycles. The variability is higher in local wintertime except for a few regions, for example, the Bay of Bengal, which shows high variability in the boreal spring and fall. Through power spectral density analysis of the seasonal SSS variability, we find that the energy differences between local winter and summer are stronger at smaller scales (<100 km). The Ka-band radar interferometry instrument on the Surface Water and Ocean Topography satellite mission will allow observation of ocean surface activities down to ∼20 km at submonthly time scales, but wave-related errors (sea state bias, aliasing, wind-driven activities, etc.) will still be a major challenge.

Plain Language Summary Many ocean processes have signatures in sea surface slope (SSS) in the 30–100 km wavelength scales, yet SSS in this band is neither well observed nor well studied globally. This paper focuses on seasonal variations of the SSS on length scales from 30 to 100 km, using satellite data collated over the past 30 years. We find high variability over strong currents and regions of rough ocean bottom topography. This variability is related to surface gravity waves and the density changes in the sub-surface of the ocean. The seasonal changes are small compared to the mean spatial variations in SSS.

1. Introduction

Satellite altimetry has revolutionized our understanding of upper-ocean circulation dynamics and sea level change. However, we still have limited understanding of sub-mesoscale to mesoscale ocean activity, defined here as variability in the 30–100 km wavelength band. This band is less well observed and less understood compared to the geostrophic band. Motions in this band have smaller scales than the O (100 km) resolution (Ballarotta et al., 2019) of the most commonly used gridded sea surface height (SSH) product, distributed by the Copernicus Marine Environment Monitoring Service (CMEMS). The spatial resolution of the CMEMS product are restricted by measurement noise and the wide separation between nadir tracks for satellite altimeters. SSH in the 30–100 km band is associated with strong eddy kinetic energy and plays an important role in the dynamics of ocean energy transfer and mixing (Ferrari & Wunsch, 2009). It contains both unbalanced wave motions (internal tides/waves, near-inertial flows) and balanced geostrophic flows. In the 30–100 km band, there are pronounced seasonal SSH variations, which are about 10% of the mean variability in amplitude (Chen & Qiu, 2021). The average variability of SSH is related primarily to the mean dynamic topography (MDT), significant wave height (SWH), lunar semi-diurnal (M2) tides, thermocline depth, and seafloor roughness (Yu et al., 2022). Among those factors, the SWH and thermocline depth have strong seasonality. Previous studies have proposed that the seasonal variability stems from (a) changes in inertia-gravity waves from the seasonally changing upper-ocean stratification (Rocha et al., 2016); or (b) changes in eddy kinetic energy from seasonally varying mixed-layer instability (Callies et al., 2016; Qiu et al., 2014; Uchida et al., 2017). These seasonality studies have the limitations of being either regional or based on model output. Our study takes a global approach, based on satellite data, using the sea surface slope (SSS) from along-track altimetry to study seasonal ocean variability and to investigate the

influence from surface waves and thermocline depth change. With more than 30 years of high-quality, repeat and non-repeat satellite altimetry data collected, the dense ground track coverage and diverse track orientations allow us to create SSS variability maps with ~10 km spatial sampling and to investigate mean, annual and semi-annual variability.

The major objective of this work is to estimate the seasonal variations (the annual and semi-annual components) of SSS variability with wavelengths from 30 to 100 km and to study the seasonal spectral characteristics of SSS variability. We try to understand the influence of the SWH and the thermocline depth on the SSS variability. We compute the SSS variability using the block median value of the absolute SSS anomaly from multiple altimeter profiles, referenced to the mean SSS. Compared to SSH, along-track slopes amplify high-wavenumber signals and "whiten" the power spectral density (PSD) by k^2, because slope is the spatial derivative of SSH. The kinetic energy tends to fall off like k^{-2} in the submesoscale range (Callies & Wu, 2019), which results in a near white PSD of SSS in the 30–100 km wavelength range. We divide the SSS variability into multiple sub-bands to investigate the seasonal spectral characteristics.

As discussed by Chen and Qiu (2021), altimeter SSH data have a white noise floor. This noise floor intersects the red-spectrum of the ocean SSH variability at wavelengths somewhat greater than 30 km. Chen and Qiu (2021) use along-track altimetry data to study the SSH in the 30–120 km band after subtracting a white noise floor for the Jason and SARAL/ALtiKa (Satellite with ARgos and ALtiKa) data (Xu & Fu, 2012). Similarly, to study the wavenumber spectra from recent missions, Vergara et al. (2019) remove a white noise floor from Jason-2 and SARAL/ALtiKa and a red noise floor from Sentinel-3. However, extrapolating the high-frequency noise floor back to lower frequencies could provide the wrong value of SSH if the white noise assumption is not valid. Moreover, it could introduce a false seasonal variation if the noise floor is linked to SWH (Lawrence & Callies, 2022), which has a large seasonal component. A major focus of our analysis is to reduce the noise by a factor >1.6 through two-pass waveform retracking (Garcia et al., 2014; Zhang & Sandwell, 2017) and careful editing. This enables us to retain shorter wavelengths in the ocean variability analysis and hopefully reduce the seasonal contamination.

The SSS variability map constructed in this study has a spatial sampling of about 10 km, and we show through correlation analysis that SSS variability is highly correlated with wave height noise at wavelengths less than 30 km (Pearson coefficient >0.5) and that the correlation is close to zero at 50-km wavelength. Thus we adopt 30 km as the shortest wavelength used in the seasonality analysis. Nevertheless there is still some correlation between SSS and SWH in the 30–50 km band. This could have two causes: (a) residual wave height noise leaks into SSS variability or (b) surface gravity waves are wind-driven, and part of the SSS variability is also wind-generated, thus leading to a strong correlation without a direct mechanistic connection between surface waves and SSS variability. We use the surface wind stress data from the version 2 Cross-Calibrated Multi-Platform (CCMP2) to help understand the impact of waves from the above two sources. A definitive understanding of the correlation between SSS and SWH will be provided by the Surface Water and Ocean Topography (SWOT) altimeter mission which will have dramatically lower SWH contamination (Fu & Ubelmann, 2014).

This paper is structured as follows: in the next section, we describe the data sets used in the study, including the SSS from satellite altimetry, high-resolution model output (Rocha et al., 2016), the SWH, the surface wind speed (WSP), and the thermocline depth. We show that SWH contaminates the shortest wavelengths (<30 km) of SSS variability. In the result section, we present the mean, annual, and semi-annual components of SSS variability in the sub-mesoscale to mesoscale bands (30–100 km). We also show the seasonal power spectra of SSS and investigate the influence of SWH and thermocline depth on the SSS variability. In Section 4 we discuss the details of the spatial and temporal variations in SSS variability, and investigate the latitude variations in terms of solar forcing and oceanographic processes.

2. Data Sets

2.1. Sea Surface Slope From Altimetry

We use the along-track profiles from Envisat, Cryosat-2, Jason 1/2, SARAL/ALtiKa and Sentinel-3A/B collected from 2001 to 2022. The altimeter data have two modes. The older altimeters operate in the standard low-resolution mode (LRM), where the radar footprint is circular and several km in diameter depending on SWH. Cryosat-2 and Sentinel-3 can operate in the synthetic aperture radar (SAR) mode, where the along-track footprint is reduced to

~250 m through synthetic aperture analysis. The noise level of the Sentinel-3 SAR altimeter is 1–2 times lower than other LRM altimeters (Ranndal et al., 2018). However, as shown in previous studies (Garcia et al., 2014; Zhang & Sandwell, 2017), the noise floor of all the LRM altimeters can be reduced by a factor of 1.5–1.7 through two-step retracking to match the precision of SAR data. Moreover these studies provide a spectral comparison between the standard 3-parameter retracking (CMEMS) and the two-step retracking. The two-step retracking method provides the largest noise reduction in the 10–45 km wavelength band which is the band of the spectral hump (Dibarboure et al., 2014). Note that the noise floor of the SARAL/ALtiKa data is nearly 2 times lower than the best SAR data from Sentinel-3 (Zhang & Sandwell, 2017). This retracking combined with careful editing, discussed next, is essential for resolving 30 km ocean variability without having to shape the spectra of the LRM data as was needed in the Chen and Qiu (2021) analysis. We push the limits to 30 km by applying a two-step waveform retracking, which makes the radar data match the precision of SAR data.

After retracking the raw waveforms, we re-estimate, and correct, sea state bias by removing 8%–10% (dependent on satellites) of SWH in the range measurements. There are two steps to edit outliers, which further improve the spatial resolution of the profiles. First, we edit 20-Hz waveform data using flags supplied with the level-1 product. In addition, waveforms having a large misfit from the Brown model and large SWH (>10 m) are excluded. These 20-Hz data are low-pass filtered using a Parks-McClellan filter with a half gain at 6.7 km wavelength and down-sampled to 5 Hz. Standard geophysical corrections are applied, including wet and dry troposphere delay, inverse barometer effect, and solid Earth and barotropic ocean tides (FES2014, Carrère et al., 2016). The corresponding slopes from geophysical corrections are small (<1 microradian) except for the barotropic ocean tide at coastal areas (Zhang et al., 2018), which are excluded in this study. Second, the 5 Hz along-track slopes are compared with the best mean SSS model (Sandwell et al., 2019), and outliers more than 3 standard deviations (typically >30 microradians) are removed. These data are further low-pass filtered with a second Parks-McClellan derivative filter with a half gain at 8.3 km wavelength to form along-track SSS. We apply local slope geoid corrections (Sandwell & Smith, 2014) and remove the mean SSS to obtain SSS anomaly profiles that reflect oceanic variability, wave height noise, and tide model error.

We are interested in the spectral characteristics and seasonality of the SSS variability. To allow for spectral analysis, we decompose the SSS variability into 10 sub-bands that are evenly spaced in the logscale wave-number domain (10.00–15.84 km, 15.84–25.12 km, 25.12–39.81 km, 39.81–63.09 km, 63.09–100.00 km, 100.00–158.48 km, 158.48–251.18 km, 251.18–398.10 km, 398.10–630.95 km, and 630.95–1000.00 km) using 1-D band-pass Gaussian filters applied to the along-track profiles. Ideally we should apply a 2-D filter to the surface slope anomalies, but only 1-D profiles are available, so our band-pass filters are sub-optimal. The results are further subdivided into 12 months for the temporal analysis assuming that the interannual variations are small. We then calculate the median of the absolute value of the filtered slope anomalies in 7 by 5 arc minute spatial bins, which represent SSS variability. These block median compilations are weighted by a polynomial function of the SWH for each satellite mission. Finally the 7' by 5' median absolute deviations are smoothed spatially using a low-pass Gaussian filter having a half gain at 200 km wavelength to further suppress noise in the monthly maps. We generate a mask to exclude regions poleward of 66°N or 60°S, land, and shallow water areas with depths less than 100 m (because of the inaccuracy of tide models around coasts). We calculate the mean, annual, and semi-annual components of the monthly SSS variability in the 30–100 km wavelength band (which roughly combines three sub-bands that have similar spatial patterns: 25–39 km, 39–63 km, and 63–100 km), and screen out regions associated with large standard deviation (>0.4 microradian) or large mean values (>0.4 microradian), where seasonal variabilities are mostly from ice change. We update the mask and apply it to all monthly data sets in the following analysis.

2.2. Impacts From Wave Height Noise

As shown in previous studies (Zhang & Sandwell, 2017), noise from ocean surface gravity waves dominates the SSH and slope for wavelengths less than 20–50 km depending on the amplitude of the SWH as well as the retracking method used for the low-level processing. To assess this SWH contamination, we compile the SWH estimates from along-track profiles using block medians in 7' by 5' bins. These are further low-pass filtered at 200 km to reduce noise. The mean SWH map (Figure 1a) shows the expected features with typically large waves >4 m in the Southern Ocean (latitudes: −60° to −35°) and low wave height (<1.5 m) in regions that are sheltered by islands from waves generated by high-latitude storms (such as the Southern California Bight or
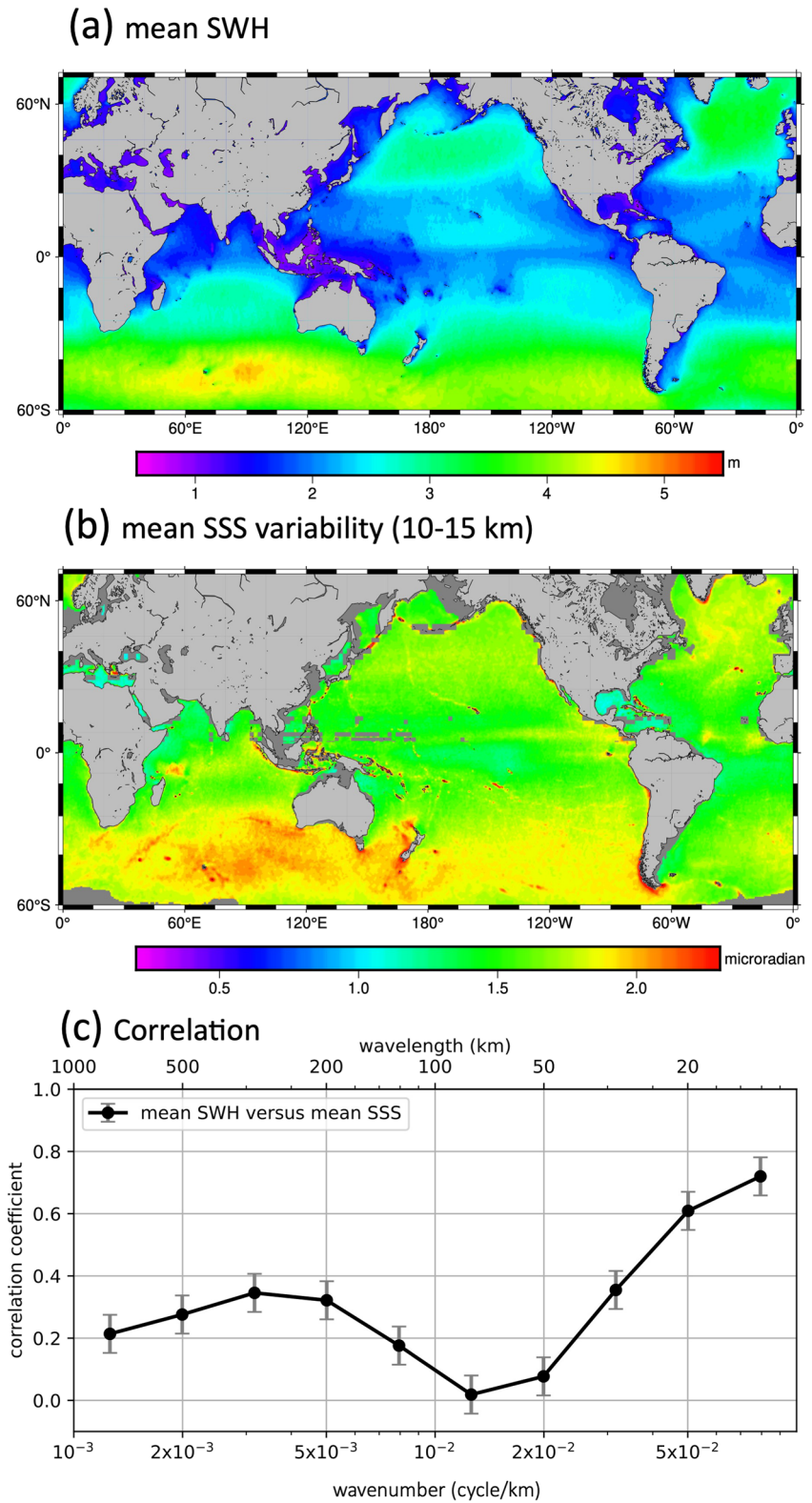
Figure 1. (a) Long-term average significant wave height (SWH) is large in the Southern Ocean and high-latitude Northern Hemisphere. (b) Sea surface slope (SSS) variability in the 10–15 km wavelength band shows similar patterns as (a), yet with more detailed patterns. (c) Correlation between average SWH and band-pass filtered SSS variability. Correlation is higher than 0.5 at wavelengths shorter than 30 km. Error bars indicate the 99% confidence interval.

the Gulf of Mexico). We are concerned that the noise from waves will contaminate the small-spatial scale SSS variability (e.g., Figure 1b), and especially their seasonal variations. We have no independent way to assess this contamination so we perform a spatial correlation based on a linear regression between the band-pass filtered SSS and SWH, as shown in Figure 1c. The SWH is highly correlated (Pearson correlation coefficient >0.5) with SSS variability for wavelengths shorter than about 30 km but poorly correlated at longer wavelengths. The high correlation suggests that the SSS variability map is dominated by noise due to ocean waves, and we exclude wavelengths less than 30 km. The same high correlation between SSS and SWH has been noted in studies where gravity anomaly has been derived from multi-mission altimetry data (Zhang et al., 2017). Those studies typically low-pass filter the SSS data at 14–18 km to reduce SWH noise while still retaining the relatively large gravity signals (∼1.0 microradian). The expected oceanographic signals are much smaller (∼0.1 microradian) than the gravity signals so the SWH contamination will extend to longer wavelengths, and more filtering is needed.

Mean slope variability in all the sub-bands is shown in Supporting Information S1 (Figure S1). Here we focus on two of the sub-bands at 100–158 km and 39–63 km wavelengths (Figure 2). The longer wavelength band (100–158 km—Figure 2a) shows all the usual features of mesoscale variability (Fu et al., 2010; Pascual et al., 2006) such as the western boundary currents, the Antarctic Circumpolar Current, and low variability in the centers of the gyres. The units of slope are in microradians (10^{-6}), where 1 microradian of slope corresponds to 63 mm of height change over a ½ wavelength of 63 km in horizontal distance, at the center of the 100–158 km wavelength band. In this band, the smallest resolvable variation is about 0.1 microradian, which corresponds to the slope of a 1 cm/s geostrophic flow in the midlatitude with a typical value of Coriolis parameter of 10^{-4} rad/s.

Many of the features seen in the shorter wavelength sub-band are new (39–63 km—Figure 2b). As expected there is high variability over eddy-intensified western boundary currents where large-scale fronts generate submesoscale variance. In addition, there is high variability associated with prominent topographic features (locations labeled in Figure 2c) such as: fracture zones (Eltanin Fracture Zone, Diamantina Fracture Zone); trenches (Aleutian Trench, Mariana Trench, Tonga Trench), spreading ridges (mid-Atlantic Ridge, Pacific-Antarctic Ridge, Southwest Indian Ridge); seamount chains (Hawaiian-Emperor seamount chain, Salas y Gómez Ridge); and continental margins (Amazon Outflow, and Mascarene plateau). While this band shows certain similarities to the M2 internal tide signatures from model output (Arbic et al., 2012), there are differences over mid-ocean ridges as well as with the intensity of internal tides. This relatively narrow band captures only part of the unbalanced wave motions from satellite altimetry observations. We also notice the strong variability in the Inter Tropical Convergence Zone (ITCZ) and the North Equatorial Countercurrents.
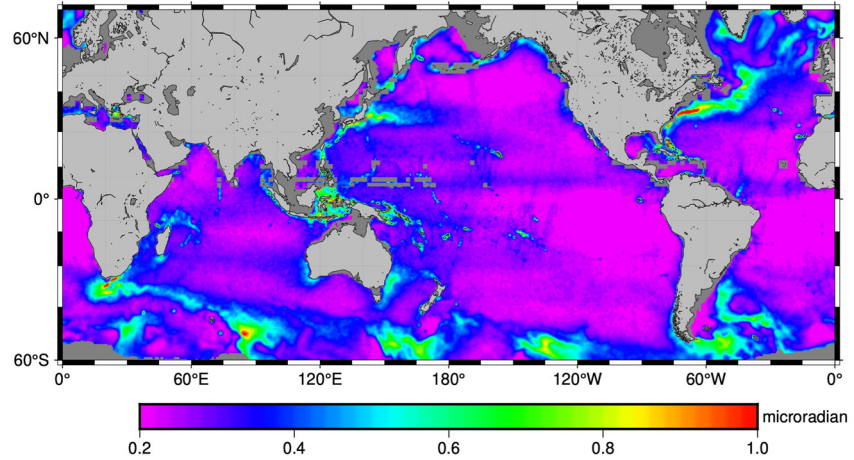
2.3. Sea Surface Slope From llc4320

We use the Estimating the Circulation and Climate of the Ocean (ECCO) Project's 1/48° MIT general circulation model with Latitude-Longitude-polar-Cap grid layout (aka llc4320, Rocha et al., 2016; Torres et al., 2018). The model is forced by 6-hourly ERA-Interim atmospheric reanalysis (Menemenlis et al., 2008) and 16 tidal components. The model has a 1/48° horizontal resolution and 90 vertical levels. We use the simulated SSH anomaly, which is referenced to the equipotential field and is noise free. We take the north-south spatial derivative of the SSH anomaly to construct the SSS anomaly, which can be directly compared with our processed SSS anomaly from satellite altimetry. We apply a 2-D bandpass filter to the hourly llc4320 SSS anomaly maps. This filter resembles the 30–100 km 1-D filter applied to the altimetry along-track SSS. We use data simulated from October 2011 to September 2012 and divide the hourly SSS data into 12 months. For each month of data, we use the median value of the absolute slope anomaly in each 7' by 5' grid to represent the slope variability. We further apply a 200 km wavelength Gaussian low-pass filter in space and obtain the monthly SSS variability maps in the 30–100 km band from llc4320 output.
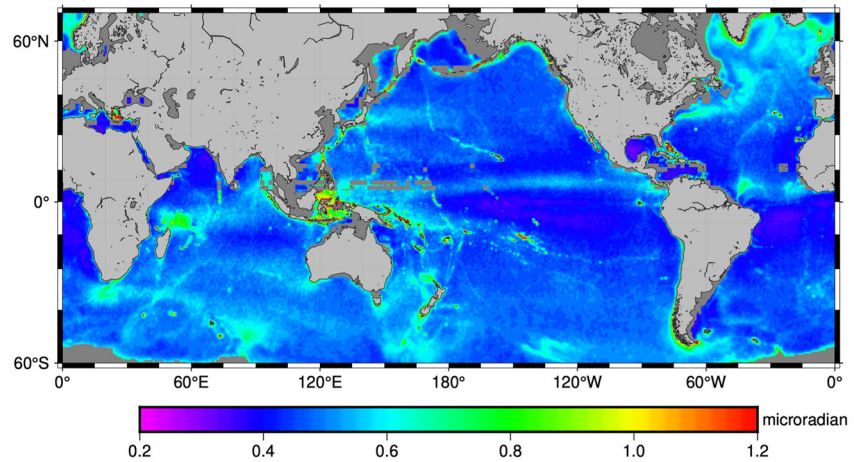
2.4. Surface Wind Speed

We adopt the CCMP2 gridded surface vector winds analysis product (Atlas et al., 2011) to create monthly WSP maps. CCMP2 is produced using satellites, moored buoys, and model wind data. We use the monthly averaged WSP provided over a 0.25° by 0.25° grid, collected from 1990 to 2018, to calculate the multi-year mean monthly WSP then downsample to 7' by 5' grids. We apply a 200 km low-pass Gaussian filter in space and apply the geographical mask to obtain monthly WSP maps that will be used in Section 3.5 in this study.
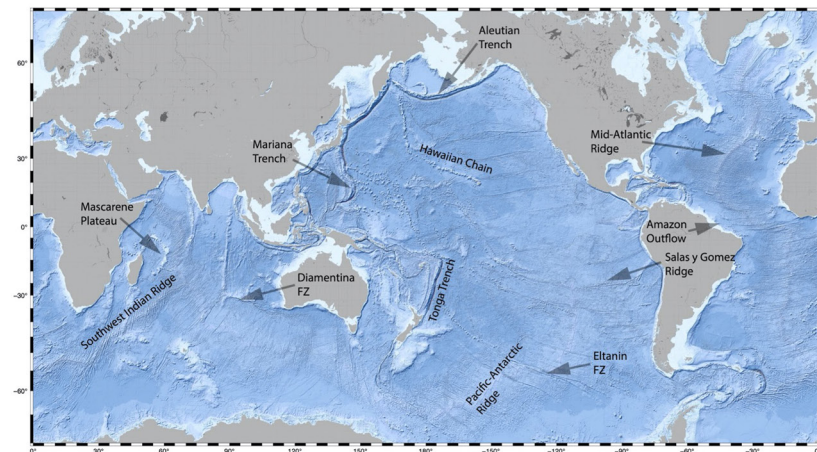
Figure 2. (a) Sea surface slope (SSS) variability in the 100–158 km wavelength band shows high variability associated with western boundary currents and the Antarctic Circumpolar current. (b) SSS variability in the 39–63 km wavelength band shows high variability over mid-ocean ridges, large seamounts chains, trenches and the Amazon shelf. Regions masked out are in gray. (c) Locations of prominent bathymetric features mentioned in text. Land is in gray and blue shading illuminates ocean topography.

2.5. Thermocline Depth

We use a climatology of monthly maximum mixed-layer depth (Holte et al., 2017) to construct the thermocline depth maps. The original data are monthly averages over the entire Argo record up to April 2022 on 1° bins, presenting an annual cycle of monthly mixed-layer properties. We apply a 200 km low-pass Gaussian filter to the maximum mixed-layer depth in space, sample the data to 7' by 5' grids, and apply the geographical mask to make the monthly thermocline depths. It has the same sampling and coverage as other data sets used in this paper.

3. Results

3.1. Seasonality: Annual Variability

For each 7' by 5' cell, we perform a point-wise least-square fit to a 5-parameter model consisting of the mean, and the sine and cosine components of the annual and semi-annual terms. We derive the amplitudes and phases, which are the months when the local periodicities reach their maxima, of the SSS variability in the 30–100 km range. We also derive the annual cycles for the SWH and the thermocline depth. At locations where amplitudes are small, the corresponding phases are not well defined.

In Figures 3a and 3b, we show the annual cycles of the SSS variability from satellite altimetry in the 30–100 km wavelength band. Here 0.1 microradian in SSS variability corresponds to 5 mm in SSH variation over a 50 km half wavelength. The annual cycle amplitude (Figure 3a) is large in the high-latitude Northern Hemisphere and the southern Indian Ocean, and their maxima are reached in local winter months (December–January in the Northern Hemisphere, June–July in the Southern Hemisphere; Figure 3b). This indicates that winter storms might be the major driving force of the SSS seasonal variability. A few regions deviate from this hemispheric-scale seasonal pattern, for example, the Philippine Sea, the Arabian Sea, the Bay of Bengal, the Mascarene Ridge, and the Northeastern Australian coasts. These regions might be driven by other strong forces that differ from the global ocean. Our altimetry annual variability (Figures 3a and 3b) resembles the annual SSH variability (30–120 km) in Chen and Qiu (2021; see their Figures 6a and 6e) using the Sentinel-3A along-track data set, where there is no noise floor removal. There are fewer similarities compared to the SARAL/ALtiKa and Jason results in Chen and Qiu (2021), where a white noise floor was subtracted from the power spectra of along-track data.

Figures 3c and 3d present the annual variability results from the llc4320 simulation data. Compared to satellite altimetry results, llc4320 shows clear signatures of individual eddies, mainly because only 1 year of simulated data is available, so long-lived eddies are visible. There are both agreements and mismatches between the annual cycles from satellite altimetry and from llc4320 (Figures 3a and 3c). For example, they both show high annual variability in regions of high geostrophic variability, in the north Atlantic Ocean and in the Southwest Indian Ridge (Figure 3a, vs. Figure 3c). The altimetry results show strong annual signals in the ITCZ and south Indian Ocean around 30°S (Figure 3a) where there are strong salinity changes, while these patterns are missing in the llc4320 annual cycle (Figure 3c). The discrepancies between satellite altimetry and llc4320 could be partially related to different sampling time spans as well as slightly different along-track directions. In llc4320, SSS is computed in the north-south direction, while satellite altimetry combines along-track slopes from multiple directions ranging from 66° to 88°. The fundamental reasons could be related to the lack of surface wave forcing and the weak constraints of large-scale features in the llc4320 simulation. The spatial patterns of the llc4320 SSS annual variability and phase (30–100 km) shown in Figures 3c and 3d are similar to spatial patterns of llc4320 SSH variability and phase (30–120 km wavelength band) found by Chen and Qiu (2021).

The annual amplitude of the SSS variability (30–100) from satellite altimetry (Figure 3a) is significantly correlated with both the annual amplitude of the SWH (Figure 3e) and the thermocline depth (Figure 3g), for example, strong amplitudes in the Kuroshio region, the north Atlantic Ocean, and the Southern Ocean. The annual phase of SSS variability (Figure 3b) is closer to the SWH (Figure 3f) than the thermocline depth (Figure 3g) except for a few regions where the thermocline depth has the largest annual changes, which implies a generally stronger link between SWH and SSS variability. Special attention should be given to the north Atlantic Ocean, where the annual amplitude of SWH is spatially uniform and reaches a maximum in January, while the thermocline annual change is significantly larger north of 50°N (red box in Figure 3g) than in mid-latitudes and peaks in February. The thermocline annual cycle maximum region (red box in Figure 3g) agrees well with the region where SSS variability reaches a maximum in February north of 50°N in the Atlantic Ocean (red box in Figure 3b). Our north Atlantic results support the hypothesis that under the same wave conditions (implying comparable wind forcing),
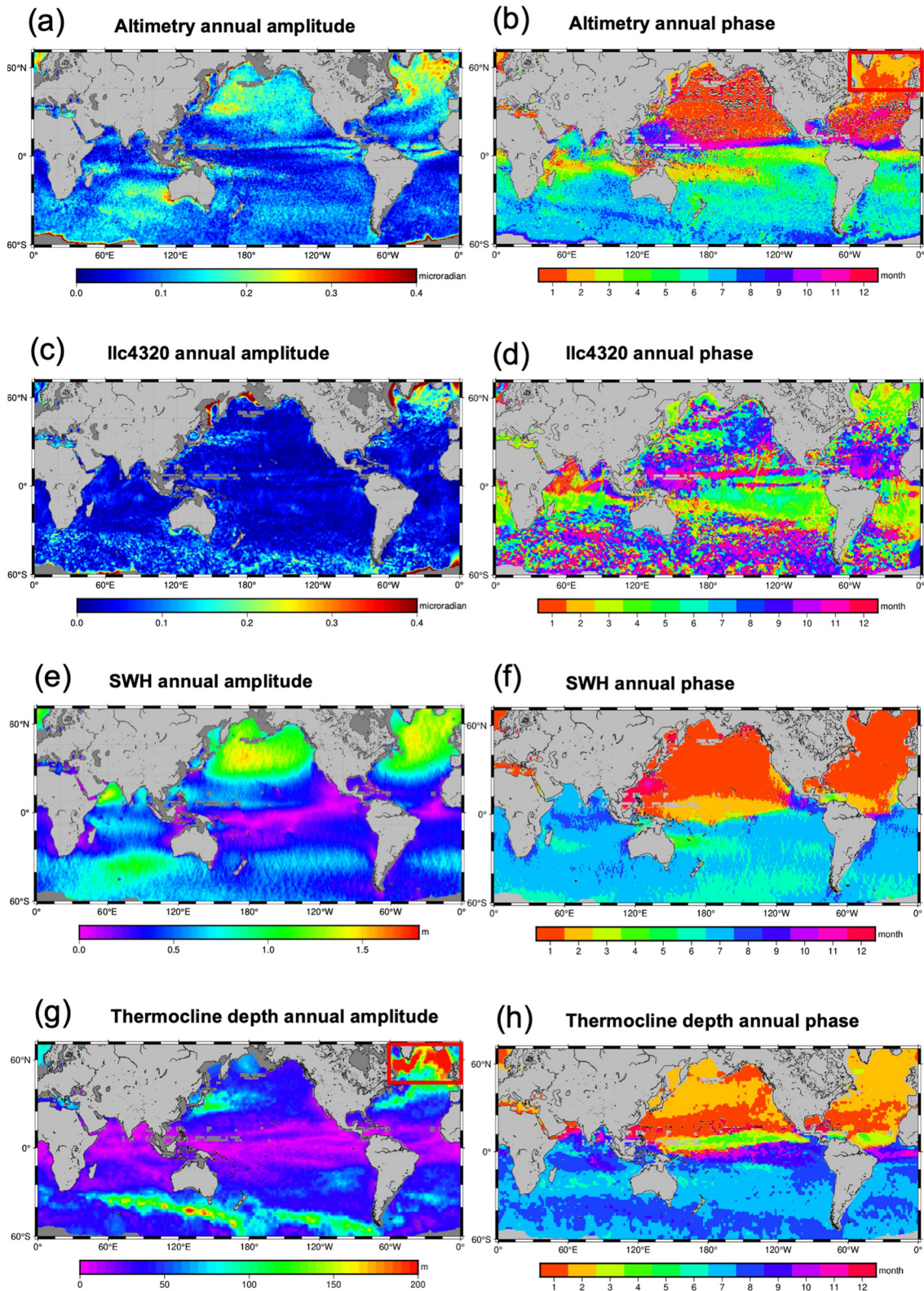
Figure 3. (a) Amplitude and (b) phase for annual sea surface slope variability in the 30–100 km wavelength band from satellite altimetry. (c) and (d) are the same as (a) and (b) but from the llc4320 output. (e) and (f) for are the annual amplitude and phase for the significant wave height. (g) and (h) are the annual amplitude and phase for the thermocline depth. Streak patterns in (e) and (f) are artifacts of the altimeter sampling patterns. Regions masked out are in gray.
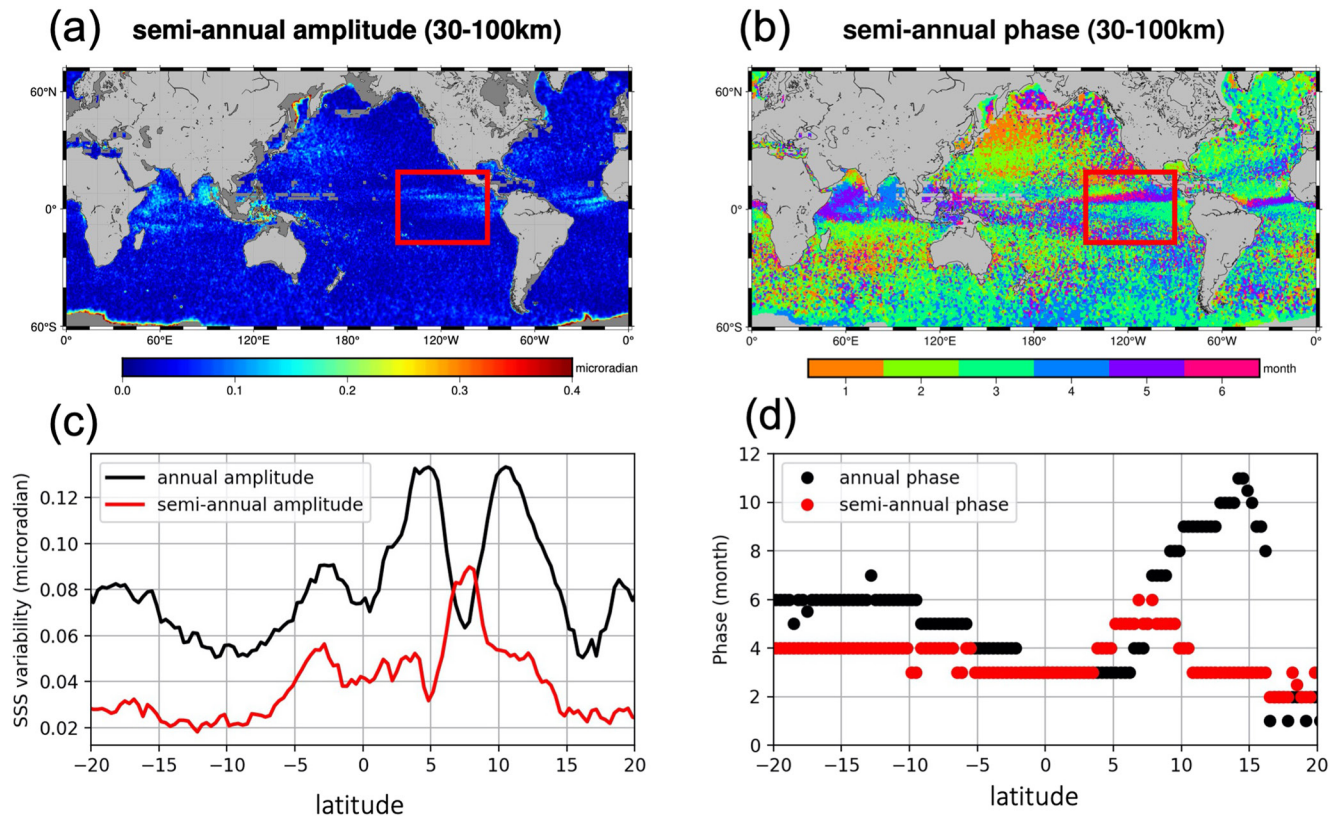
Figure 4. The amplitude (a) and phase (b) for semi-annual sea surface slope variability in the 30–100 km wavelength band from satellite altimetry. Regions masked out are in gray. Panels (c) and (d) show the amplitude and phase along a meridional profile averaged over 150°W to 90°W as shown in the red boxes in (a) and (b).

a deeper thermocline promotes more sub-mesoscale SSS variability. Under this hypothesis, we expect to see that the time series of thermocline depth leads the sub-mesoscale SSS variability in time, probably on the order of a few weeks, in regions like the Atlantic Ocean north of 50°N. In contrast, within the ITCZ in the tropical Pacific and Atlantic Oceans, both the SWH and the thermocline depth show low annual variability, which disagrees with the high SSS variability.

3.2. Seasonality: Semi-Annual Variability

We present the semi-annual cycle of the SSS variability (30–100 km) from satellite altimetry in Figures 4a and 4b. Semi-annual variations are mostly confined within ±15° latitude (Figure 4a), and they are highly correlated with principal monsoon regions (Saha, 2009). We identify strong semi-annual variations in the Arabian Sea and the Bay of Bengal, and the driving forces could be related to the South Asian monsoon's semi-annual occurrence and the salinity variability (Drushka et al., 2019).

In the Pacific and Indian Ocean tropics, the annual and semi-annual components of the SSS variability are strong and orthogonal in space. We show the annual/semi-annual amplitude and phase along a meridional profile zonally averaged over 150°W–90°W in Figures 4c and 4d. The annual cycle shows double peaks around 4°N and 11°N, with maxima in March or September. The semi-annual cycle peaks around 7°N in June and December. These results are consistent with a spatially oscillating pattern in SSS variability, centered around 7°N and migrating in the meridional direction at an annual period. It is highly correlated with the marine ITCZ, which undergoes a regular seasonal migration reaching its northernmost position during late boreal summer (August–September) and approaching the equator during boreal winter (February–March), passing the central latitude twice a year (Koutavas & Lynch-Stieglitz, 2004).

In contrast to the altimeter results, in the llc4320 model, the semi-annual amplitude resembles the annual amplitude, and the phase has no clear pattern. The annual and semi-annual cycles with poorly defined phases might be

Table 1
The Global Median Value of the Mean, the Annual/Semi-Annual Amplitude of the Sea Surface Slope Variability, and the Median Fraction of Variance Explained in Three Wavelength Bands

SSS—band (km)	Mean (µrad)	Annual (µrad)	Semi-annual (µrad)	FVE (%)
10–30	2.52	0.27	0.083	85.7
30–100	0.91	0.096	0.036	79.0
100–1,000	0.65	0.057	0.037	58.0

hard to differentiate given that only 1 year of data is available. We show the comparison of the mean SSS variability (30–100 km) from satellite altimetry and llc4320 in Supporting Information S1 (Figure S2) and show the semi-annual variations from llc4320 in Supporting Information S1 (Figure S3).

3.3. Seasonality: Assessment

We next assess the success of our fitted seasonal cycles. We run the 5-parameter least-squares fitting with the assumption that the annual and semi-annual variations contain the majority of SSS variance and they undergo sinusoidal cycles. To evaluate the least-squares fitting, we adopt the metric of fraction of variance explained (FVE) (Colosi et al., 2021; Draper & Smith, 1998), defined as:

$$FVE = 1 - \frac{\sum\limits_{i=1}^{N} (y_i - \hat{y}_i)^2}{\sum\limits_{i=1}^{N} (y_i - \overline{y})^2}$$

where y_i is the ith observation, $\hat{y}_i$ is the ith estimate, and $\overline{y}$ is the mean value. N is the number of total observations, which is 12 in this study. We assume that each estimate has the same uncertainty. The global maps of FVE for each sub-band of the SSS variability from satellite altimetry are provided in Figure S4 of the Supporting Information S1. In general, the percent of variance explained by the least-squares fit is high in regions of high variability and low in regions of small annual amplitude. SSS variability with shorter wavelengths is associated with higher FVE, indicating that the submesoscale to mesoscale bands (30–100 km) are mostly governed by annual and semi-annual cycle processes. The complete set of plots showing the mean, the annual and semi-annual amplitudes of SSS variability using satellite altimetry data, as well as the FVE maps are provided in Figures S1, S4, S5, and S6 of the Supporting Information S1.

3.4. Spectral Analysis

In this section, in order to highlight different dynamical features, we present the PSD from satellite altimetry as well as time series in six selected regions. Table 1 summarizes representative statistics for the global median value of the mean, annual/semi-annual amplitude of the SSS variability, and the FVE in three wavelength bands: the 10–30 km band which is contaminated by waves; the 30–100 km submesoscale band; and the >100 km mesoscale band. Table 1 allows magnitude comparisons between the annual, semi-annual, and mean SSS variability. Because we use different bandwidths, we avoid comparison across different wavelength bands. We find that the seasonal components are small: the annual amplitude is ~10%, and semi-annual amplitude is ~4% of the mean variability. The median FVE by the annual and semi-annual least-squares fit is 85.7% at the short wave band, then decreases to 58.0% at mesoscales. This means that mesoscale SSS variability is more complicated than a simple seasonal cycle.

We discuss the seasonal PSD in six selected regions: the Kuroshio region (140°/190°/30°/45°); the North Atlantic Ocean (320°/350°/56°/66°); the California coast (23°/239°/29°/42°); the Bay of Bengal (80°/100°/0°/20°); the west of Australia (60°/120°/-45°/-30°); and the Atlantic equatorial area (320°/345°/0°/15°) and present the PSD in Figure 5. The six regions are selected to highlight a range of specific dynamical features: (a) there are consistent strong geostrophic currents over the Kuroshio region; (b) the Atlantic Ocean north of 50°N is associated with the largest thermocline depth change; (c) there are strong local winds in late boreal spring at the California coast; (d) the semi-annual SSS cycle dominates the Bay of Bengal; (e) the west of Australia demonstrates intense SSS variability and salinity change; (f) both the annual and semi-annual SSS cycles are strong in the Atlantic equatorial area.

We use 3-month intervals to compute the seasonal SSS variability, that is, December-January-February for winter, March-April-May for spring, June-Jul -August (June-July -August) for summer, and September-October -November for fall in the Northern Hemisphere. For each wavelength band, we square the median value of the
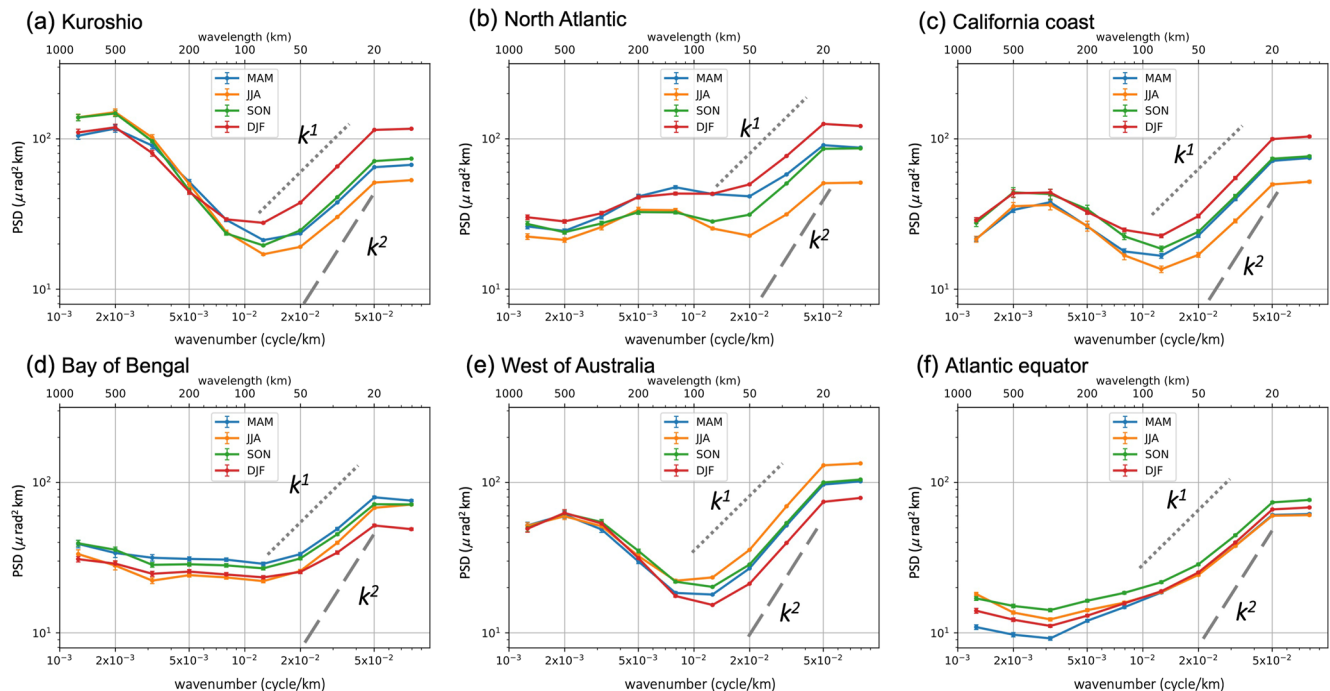
Figure 5. The power spectral density of the seasonal sea surface slope variability in (a) the Kuroshio region; (b) the north Atlantic Ocean; (c) the California coast; (d) the Bay of Bengal; (e) the west of Australia; and (f) the Atlantic equatorial area. The 99% confidence intervals are provided at the center of each band. The k and k^2 spectral slopes are indicated for reference.

absolute seasonal SSS anomaly in the selected area, then divide it by the bandwidth to represent the seasonal PSD. The 10 wavelength sub-bands (10.00–15.84 km, 15.84–25.12 km, 25.12–39.81 km, 39.81–63.09 km, 63.09–100.00 km, 100.00–158.48 km, 158.48–251.18 km, 251.18–398.10 km, 398.10–630.95 km, and 630.95–1000.00 km) are equally spaced in the logscale wavenumber domain, and the band widths are larger at high wavenumbers. The result is shown in Figure 5, where PSD has units of microradian 2 km. PSD does not depend on the choice of bandwidth, so we can compare the energy across different wavelengths. Error bars indicate the 99% confidence interval in the selected area, and the k^1 and k^2 spectral slopes are labeled in the 20–100 km range.

The six selected regions show blue spectra at high wavenumbers ($>10^{-2}$ cycles/km), which means that the SSS variability in the 30–100 km band is dominated by energy in the shortest wavelengths. The PSD of SSS in the 20–50 km wavelength range basically follows a k^1 or even smaller spectral slope, which suggests a roughly k^{-1} SSH spectrum. This means that our data processing method has effectively reduced the white measurement noise in the satellite altimetry along-track observations. At high wavenumbers ($>10^{-2}$ cycles/km), the energy in general reaches a maximum in local winter and minimum in local summer (Figures 5a,5b,5c, and 5e). This agrees with Figure 2b showing that the annual cycles reach their maxima in local winter within the 30–100 km band with a few exceptions including the Bay of Bengal (Figure 5d). At the Bay of Bengal where semi-annual variability dominates, the energy is high in the boreal spring and fall. The Bay of Bengal also demonstrates higher energy in the summer at high wavenumbers ($>10^{-2}$ cycles/km), possibly under the influence of strong surface winds. The cross-season energy differences are smaller at low wavenumbers ($<10^{-2}$ cycles/km) in general.

3.5. Impacts From SWH and Thermocline Depth

While the high correlation between SWH and SSS (<30 km) is suggestive of SWH noise leakage into the SSS variability, there are also good physical reasons why SSS variability could be correlated with SWH. Winds and wave heights are highly correlated. Surface gravity waves are generated by the friction between wind and water, and upper-ocean geostrophic currents are established in response to winds (e.g., Stommel, 1948). If both the SSS and SWH are responding to wind forcing then there should be a strong correlation in their time series. The
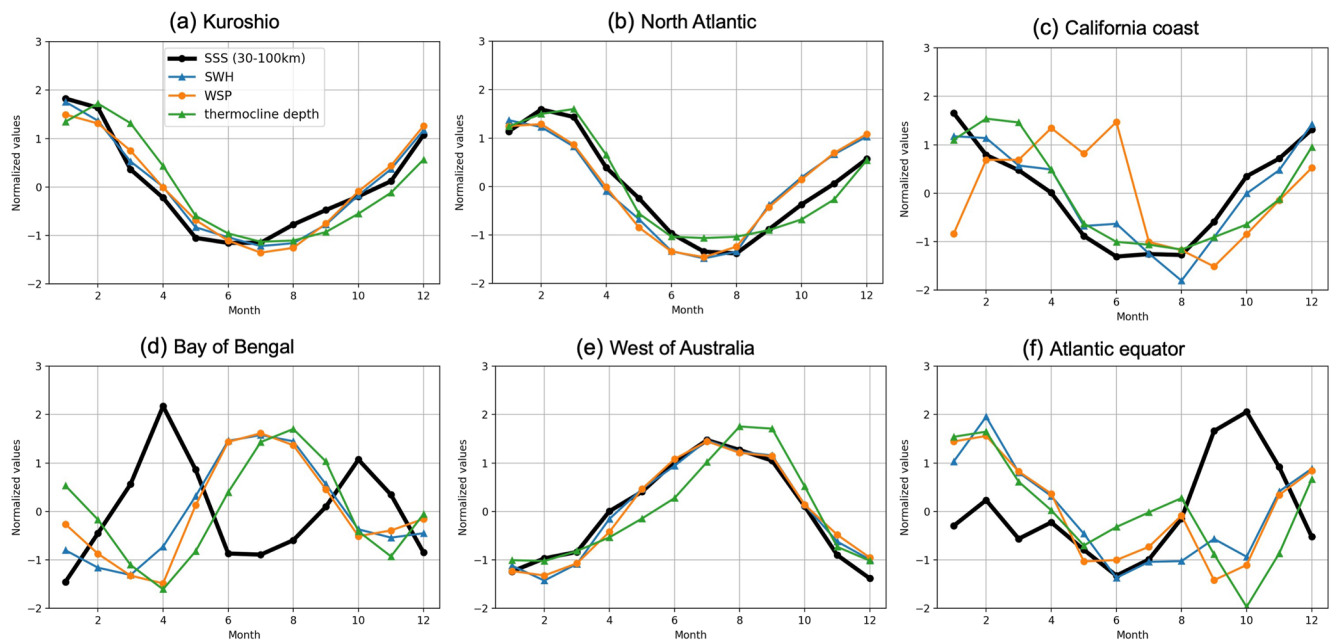
Figure 6. The normalized time series of the mean sea surface slope variability (30–100 km, thick black line with rounds dots), significant wave height (blue line with triangle dots), wind speed (orange line with round dots), and the thermocline depth (green line with triangle dots) in (a) the Kuroshio region; (b) the north Atlantic Ocean; (c) the California coast; (d) the Bay of Bengal; (e) the west of Australia; and (f) the Atlantic equatorial area.

thermocline depth as a secondary driving factor, as shown in Section 3.1, promotes SSS variability by storing potential energy, which can be converted to eddy kinetic energy (Callies et al., 2016; Qiu et al., 2014; Uchida et al., 2017). To further understand the impact from waves and the thermocline depth, in Figure 6 we plot the normalized time series of the mean SSS variability in the 30–100 km wavelength band, SWH, WSP, and thermocline depths in the six regions as introduced in Section 3.4.

For each region, we compare the time series of SSS variability (30–100 km) from satellite altimetry, SWH, WSP, and the thermocline depth. In the west of Australia, the SSS variability, SWH, and WSP undergo correlated annual cycles that peak in July (Figure 6e). The Kuroshio region (Figure 6a) and the North Atlantic Ocean (Figure 6b) show similar patterns except that there are phase differences between the SSS and SWH/WSP (leading/lagging by 1 month). In the Kuroshio region (Figure 6a), the thermocline depth leads the SSS by 1 month, which agree s with the numerical study of Dong et al. (2020). The Atlantic Ocean north of 50°N (Figure 6b) witnesses the largest thermocline depth annual cycle, reaching its minimum around July. Shallower thermocline depths are hypothesized to be less effective at storing potential energy and thus less effective in promoting sea surface variability. This is consistent with the fact that SSS variability reaches its minimum 1 month afterward. Regions with weak thermocline depth changes may not be impacted as much and are thus not discussed here. The California coast experiences strong local winds in late spring, yet the SWH and SSS are not affected (Figure 6c). In the Bay of Bengal (Figure 6d), the SSS variability shows semi-annual cycles peaking in boreal spring and fall, while the SWH and WSP reach maxima in July. The anti-correlation indicates that winds and surface waves are not the sole drivers of the ocean sub-mesoscale variability, and local factors might have stronger influences. For example, the northern Bay of Bengal has strong submesoscale salinity variability, influenced by the Ganges-Brahmapputra River outflows (Gordon et al., 2016). This region is also influenced by the South Asian monsoon's semi-annual occurrence. The Atlantic equatorial area shows a strong SSS peak in October which is in phase neither with SWH nor with WSP. The different variability patterns between the SSS variability and SWH/WSP in the Bay of Bengal (Figure 6d) and the Atlantic equator (Figure 6f) indicate that surface waves/winds are not the only driving factor of the SSS variability. The different timing between SSS and SWH in the Kuroshio (Figure 6a) and the north Atlantic Ocean (Figure 6b) shows that there are real energetics in the upper ocean other than signal leakage from SWH in the 30–100 km wavelength band.

4. Discussion and Conclusions

Repeat-pass altimetry cannot resolve the small wavelength (<150 km) spatial variations in ocean surface height/slope variability for three reasons: first, the smallest track spacing is ~80 km (Envisat) at the equator; second, errors in the marine geoid/slope can dominate the residual SSH/SSS in the gaps between the repeat tracks; and third, ocean waves produce white noise in the SSH/SWH, known as a noise hump in the PSD of SSH, which commonly dominates the signal at wavelengths <~50 km. Since 2014, the marine geoid/gravity community (Andersen & Knudsen, 2019; Li et al., 2022; Sandwell et al., 2019; Zhang et al., 2020) has been focused on improvements in spatial resolution and accuracy by addressing each of these issues. The quantity and quality of non-repeat and gap-filling altimeter data has increased dramatically with CryoSAT-2, Jason-1/2 geodetic phases, the SARAL/AltiKa geodetic mission, and the new repeat track of the Sentinel-3A/B satellites. In addition, the short-wavelength altimeter noise for the standard LRM products can be reduced to the noise level of the latest SAR mission products through 2-pass retracking (Garcia et al., 2014; Zhang & Sandwell, 2017) and careful editing. Of course, the recent launched SWOT altimeter mission will, hopefully, resolve 20 km spatial wavelengths at a high temporal sampling to reveal a wealth of new ocean dynamics (Fu & Ubelmann, 2014). Here we reprocessed the available repeat and non-repeat altimeter data, collected over the past 30 years, using the 2-step retracking to reduce the noise hump, to begin to resolve the small spatial patterns at a low temporal resolution (mean, 12, 6 months). We worked with the original trackline altimeter data, as residual SSS, to pre-whiten the red spectrum of the ocean dynamic signals which enables along-track, band-pass filtering.

Our overall analysis has 10 spatial bands between wavelengths of 10 and 1,000 km and three temporal bands: mean, annual, and semi-annual (i.e., 5 coefficients). In many cases, the individual bands have low signal-to-noise ratios so we combined the spatial bands into three groups. Spatial variations in mesoscale variability (>100 km wavelength) are discussed and analyzed in many previous publications (e.g., Qiu et al., 2014; Sasaki et al., 2017) so they are not repeated here. We showed through correlation analysis that SWH noise dominates the residual SSS between wavelengths of 10–30 km, so these bands are not considered further. The remaining bands from 30 to 100 km wavelength have sufficient signal-to-noise ratios to reveal new signals at mean, annual, and semi-annual timescales. The three sub-bands in the 30–100 km range (25–39 km, 39–63 km, and 63–100 km) all have similar spatial patterns, so they were combined to improve the recovery of the annual/semi-annual signals. We also calculate the seasonal components of other wavelength bands (39–100 km and 50–100 km) and they show similar spatial patterns as the 30–100 km. Thus, we think that 30–100 km is a robust choice. The 30–100 km submesoscale band contains both unbalanced wave motions (internal tides/waves, near-inertial flows) and balanced geostrophic flows, and which one dominates is geographically dependent (Chen & Qiu, 2021; Chereskin et al., 2019; Qiu et al., 2017, 2018).

4.1. Interpretation of the Mean SSS

The analysis of the long-term average of the SSS variability in the 30–100 km wavelength band is more completely discussed in a related publication (Yu et al., 2022), so only the highlights are discussed here. That study used a machine learning approach to rank the dominant environmental factors that influence the SSS variability over the 30–100 km band, which are distance to the nearest thermocline boundary, SWH, MDT, MDT gradient, seafloor roughness, M2 tidal speed, K1 tidal amplitude, and stratifications. The stratification is closely related to the thermocline depth. The correlation with the SWH and the thermocline depth, and especially the annual variations, will be discussed more completely below. In this study, we also investigate the annual and semi-annual variations (amplitude and phase) in SSS in the 30–100 km wavelength band. An initial finding is that the annual amplitude is one tenth the mean amplitude, and the semi-annual amplitude is 1/25th the mean amplitude. This makes the interpretation of these temporal signals both challenging and new.

4.2. Interpretation of the Annual SSS

One new finding of our seasonal analysis is that SSS variability is correlated with both the SWH and the thermocline depth. We expect there will be some SWH noise leakage into SSS at longer wavelengths (>30 km). To address this issue, we present the spatial correlation between the SSS variability and SWH as well as the thermocline depth in Figure 7. The SSS variability at smaller wavelengths is associated with more seasonal variability as summarized in Table 1. The correlations between annual components are higher compared to the
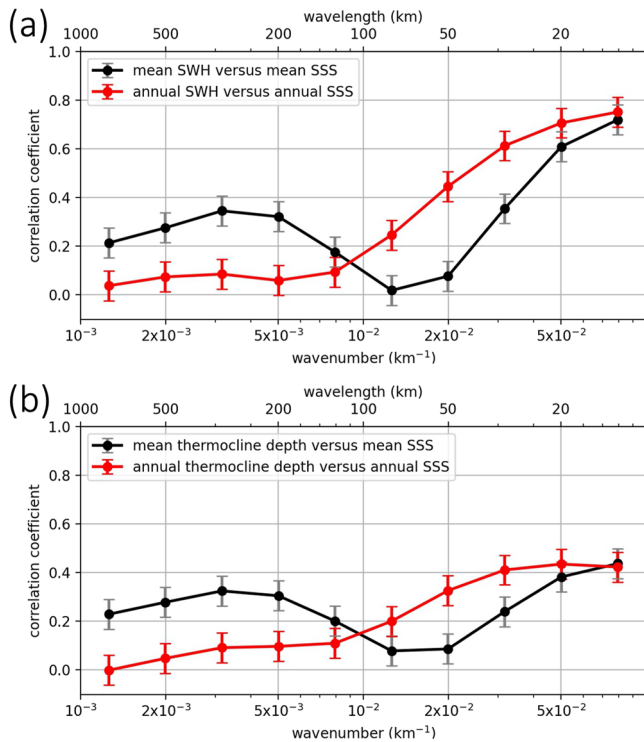
Figure 7. (a) Correlation between the mean significant wave height (SWH) and mean band-pass filtered sea surface slope (SSS) (black curve); correlation between the annual amplitude of SWH and annual amplitude of the band-pass filtered SSS (red curve); (b) same as (a) but for the correlation between the thermocline depth and the SSS. Error bars indicate the 99% confidence interval.

mean components at short wavelengths (<100 km), and lower at longer wavelengths (>100 km). The correlation with thermocline depth is smaller compared to the correlation with SWH at sub-mesoscales (<100 km), which supports Figure 3 result that the annual phase of the SSS variability agrees better with SWH. The differences in the annual phase (Figure 3) and the time series of SSS and SWH/WSP (Figure 6) indicate that the SSS variability (30–100 km) is not entirely driven by wind or surface waves, nor is it contaminated by SWH leakage. In the future, in situ measurements from wave buoys can help to evaluate the influence from SWH.

There are two competing hypotheses for the influence of the thermocline depth on the ocean surface variability. One hypothesis predicts that the deeper thermocline associated with less stratified water stores more potential energy, which can be transferred to more eddy kinetic energy and create more small-scale surface motions (Callies et al., 2016; Qiu et al., 2014; Sasaki et al., 2014; Uchida et al., 2017). The second hypothesis is that shallower thermoclines have thinner upper layers. Momentum from the atmosphere can be transferred to a thinner upper layer in a more effective way and make the ocean surface move faster (Peng et al., 2022). For geostrophic motions represented by SSS variability and for the time scales resolved in the altimeter record, our results support the first hypothesis that in the local winter when the thermocline is deeper, the SSS variability is stronger, though the thermocline depth is a secondary driving factor compared to the SWH. Baroclinic mixed-layer instabilities, arising from density gradients, can restratify the system and lead to turbulence, converting potential energy into eddy kinetic energy. In this study we focus on the seasonality in the 30–100 km spatial scale and our attention is not on any specific ocean activities in this band.

4.3. Interpretation of the Annual/Semi-Annual SSS

A significant new finding of our combined annual/semi-annual analysis is that there is an equatorial region of high SSS variability that essentially follows the atmospheric ITCZ. This signal is most prominent in the Pacific and Atlantic Oceans, where it appears as a north-south annual migration of the high variability bands. When this is modeled as combined annual and semi-annual signals, the two components have spatially orthogonal patterns. At the central latitude (~7°N) where the SSS variability peak passes twice a year in June and December, the semi-annual amplitude is the largest; at the two boundaries (~4°N and ~11°N) where the peak passes once a year in February–March and August–September, separately, there are strong annual signals. We propose that this pattern is related to the seasonal marine ITCZ shift, driven by interhemispheric solar heating differences and the cross-equatorial atmospheric energy heating (Bischoff & Schneider, 2016). The interannual migration of the ITCZ is related to El Niño-Southern Oscillation (Bischoff & Schneider, 2016), which modulates the sea surface temperature at interannual scales, but our analysis has not been constructed to analyze interannual time scales.

4.4. Future Work Needed to Resolve These Issues

The SWOT wide-swath altimetry mission, which was launched in late 2022, will characterize the ocean sub-mesoscale activities at spatial scales larger than 20 km and answer some fundamental questions about the formation and dynamics of sub-mesoscale activities and ocean circulation (Fu & Ubelmann, 2014). But wave-related errors (sea state bias, aliasing, wind-driven activities, etc.) will still be a major issue that SWOT has to face. SWOT's an initial phase of 90 1-day repeats will allows us to evaluate the along-track and cross-track slope accuracy over wellcharted, large seamounts (i.e., Foundation seamounts, South Pacific), where we have a mean SSS model with accuracy better than 1 microradian at wavelengths at a 10 km wavelength resolution. We expect the accuracy will primarily depend on the SWH, and studying the accuracy under different wave conditions will help us to understand the influence of wave-related errors.

Data Availability Statement

The sea surface slope and significant wave height data are available through: https://doi.org/10.5281/zenodo.7311420. The surface wind speed data are from: https://www.remss.com/measurements/ccmp/. The thermocline depth data are from: http://mixedlayer.ucsd.edu/. The llc4320 model output is downloaded using the python llcreader module (https://xmitgcm.readthedocs.io/en/latest/llcreader.html) via the ECCO data portal: https://data.nas.nasa.gov/ecco/data.php?dir=/eccodata/llc_4320.

References

Andersen, O. B., & Knudsen, P. (2019). The DTU17 global marine gravity field: First validation results. In S. Mertikas & R. Pail (Eds.), *Fiducial reference measurements for altimetry, international association of geodesy symposia* (Vol. 150, pp. 83–87). Springer: Berlin/Heidelberg.

Arbic, B. K., Richman, J. G., Shriver, J. F., Timko, P. G., Metzger, E. J., & Wallcraft, A. J. (2012). Global modeling of internal tides: Within an eddying ocean general circulation model. *Oceanography*, *25*(2), 20–29. https://doi.org/10.5670/oceanog.2012.38

Atlas, R., Hoffman, R. N., Ardizzone, J., Leidner, S. M., Jusem, J. C., Smith, D. K., & Gombos, D. (2011). A cross-calibrated, multiplatform ocean surface wind velocity product for meteorological and oceanographic applications. *Bulletin of the American Meteorological Society*, *92*(2), 157–174. https://doi.org/10.1175/2010bams2946.1

Ballarotta, M., Ubelmann, C., Pujol, M. I., Taburet, G., Fournier, F., Legeais, J. F., et al. (2019). On the resolutions of ocean altimetry maps. *Ocean Science*, *15*(4), 1091–1109. https://doi.org/10.5194/os-15-1091-2019

Bischoff, T., & Schneider, T. (2016). The equatorial energy balance, ITCZ position, and double-ITCZ bifurcations. *Journal of Climate*, *29*(8), 2997–3013. https://doi.org/10.1175/jcli-d-15-0328.1

Callies, J., Flierl, G., Ferrari, R., & Fox-Kemper, B. (2016). The role of mixed-layer instabilities in submesoscale turbulence. *Journal of Fluid Mechanics*, *788*, 5–41. https://doi.org/10.1017/jfm.2015.700

Callies, J., & Wu, W. (2019). Some expectations for submesoscale sea surface height variance spectra. *Journal of Physical Oceanography*, *49*(9), 2271–2289. https://doi.org/10.1175/jpo-d-18-0272.1

Carrère, L., Lyard, F., Cancet, M., Guillot, A., & Picot, N. (2016). FES 2014, a new tidal model—Validation results and perspectives for improvements. In *Proceedings of the ESA living planet symposium* (pp. 9–13).

Chen, S., & Qiu, B. (2021). Sea surface height variability in the 30–120 km wavelength band from altimetry along-track observations. *Journal of Geophysical Research: Oceans*, *126*(4), e2021JC017284. https://doi.org/10.1029/2021jc017284

Chereskin, T. K., Rocha, C. B., Gille, S. T., Menemenlis, D., & Passaro, M. (2019). Characterizing the transition from balanced to unbalanced motions in the southern California current. *Journal of Geophysical Research: Oceans*, *124*(3), 2088–2109. https://doi.org/10.1029/2018jc014583

Colosi, L. V., Villas Bôas, A. B., & Gille, S. T. (2021). The seasonal cycle of significant wave height in the ocean: Local versus remote forcing. *Journal of Geophysical Research: Oceans*, *126*(8), e2021JC017198. https://doi.org/10.1029/2021jc017198

Dibarboure, G., Boy, F., Desjonqueres, J. D., Labroue, S., Lasne, Y., Picot, N., et al. (2014). Investigating short-wavelength correlated errors on low-resolution mode altimetry. *Journal of Atmospheric and Oceanic Technology*, *31*(6), 1337–1362. https://doi.org/10.1175/jtech-d-13-00081.1

Dong, J., Fox-Kemper, B., Zhang, H., & Dong, C. (2020). The seasonality of submesoscale energy production, content, and cascade. *Geophysical Research Letters*, *47*(6), e2020GL087388. https://doi.org/10.1029/2020gl087388

Draper, N. R., & Smith, H. (1998). *Applied regression analysis* (Vol. 326). John Wiley & Sons.

Drushka, K., Asher, W. E., Sprintall, J., Gille, S. T., & Hoang, C. (2019). Global patterns of submesoscale surface salinity variability. *Journal of Physical Oceanography*, *49*(7), 1669–1685. https://doi.org/10.1175/jpo-d-19-0018.1

Ferrari, R., & Wunsch, C. (2009). Ocean circulation kinetic energy: Reservoirs, sources, and sinks. *Annual Review of Fluid Mechanics*, *41*(1), 253–282. https://doi.org/10.1146/annurev.fluid.40.111406.102139

Fu, L. L., Chelton, D. B., Le Traon, P. Y., & Morrow, R. (2010). Eddy dynamics from satellite altimetry. *Oceanography*, *23*(4), 14–25. https://doi.org/10.5670/oceanog.2010.02

Fu, L. L., & Ubelmann, C. (2014). On the transition from profile altimeter to swath altimeter for observing global ocean surface topography. *Journal of Atmospheric and Oceanic Technology*, *31*(2), 560–568. https://doi.org/10.1175/jtech-d-13-00109.1

Garcia, E. S., Sandwell, D. T., & Smith, W. H. (2014). Retracking CryoSat-2, Envisat and Jason-1 radar altimetry waveforms for improved gravity field recovery. *Geophysical Journal International*, *196*(3), 1402–1422. https://doi.org/10.1093/gji/ggt469

Gordon, A. L., Shroyer, E. L., Mahadevan, A., Sengupta, D., & Freilich, M. (2016). Bay of Bengal: 2013 northeast monsoon upper-ocean circulation. *Oceanography*, *29*(2), 82–91. https://doi.org/10.5670/oceanog.2016.41

Holte, J., Talley, L. D., Gilson, J., & Roemmich, D. (2017). An Argo mixed layer climatology and database. *Geophysical Research Letters*, *44*(11), 5618–5626. https://doi.org/10.1002/2017GL073426

Koutavas, A., & Lynch-Stieglitz, J. (2004). Variability of the marine ITCZ over the eastern Pacific during the past 30,000 years. In *The Hadley circulation: Present, past and future* (pp. 347–369). Springer.

Lawrence, A., & Callies, J. (2022). Seasonality and spatial dependence of meso-and submesoscale ocean currents from along-track satellite altimetry. *Journal of Physical Oceanography*, *52*(9), 2069–2089. https://doi.org/10.1175/jpo-d-22-0007.1

Li, Z., Guo, J., Ji, B., Wan, X., & Zhang, S. (2022). A review of marine gravity field recovery from satellite altimetry. *Remote Sensing*, *14*(19), 4790. https://doi.org/10.3390/rs14194790

Menemenlis, D., Campin, J. M., Heimbach, P., Hill, C., Lee, T., Nguyen, A., et al. (2008). ECCO2: High resolution global ocean and sea ice data synthesis. *Mercator Ocean Quarterly Newsletter*, *31*, 13–21.

Pascual, A., Faugère, Y., Larnicol, G., & Le Traon, P. Y. (2006). Improved description of the ocean mesoscale variability by combining four satellite altimeters. *Geophysical Research Letters*, *33*(2), L02611. https://doi.org/10.1029/2005gl024633

Peng, Q., Xie, S. P., Wang, D., Huang, R. X., Chen, G., Shu, Y., & Liu, W. (2022). Surface warming-induced global acceleration of upper ocean currents. *Science Advances*, *8*(16), eabj8394. https://doi.org/10.1126/sciadv.abj8394

Qiu, B., Chen, S., Klein, P., Sasaki, H., & Sasai, Y. (2014). Seasonal mesoscale and submesoscale eddy variability along the North Pacific subtropical countercurrent. *Journal of Physical Oceanography*, *44*(12), 3079–3098. https://doi.org/10.1175/jpo-d-14-0071.1

Qiu, B., Chen, S., Klein, P., Wang, J., Torres, H., Fu, L. L., & Menemenlis, D. (2018). Seasonality in transition scale from balanced to unbalanced motions in the world ocean. *Journal of Physical Oceanography*, *48*(3), 591–605. https://doi.org/10.1175/jpo-d-17-0169.1

Qiu, B., Nakano, T., Chen, S., & Klein, P. (2017). Submesoscale transition from geostrophic flows to internal waves in the northwestern Pacific upper ocean. *Nature Communications*, *8*(1), 14055. https://doi.org/10.1038/ncomms14055

Ranndal, H., Andersen, O. B., & Knudsen, P. (2018). Global and regional evaluation of the first year of Sentinel-3. *Fiducial Reference Measurements for Altimetry*, 89–96.

Rocha, C. B., Gille, S. T., Chereskin, T. K., & Menemenlis, D. (2016). Seasonality of submesoscale dynamics in the Kuroshio extension. *Geophysical Research Letters*, *43*(21), 11–304. https://doi.org/10.1002/2016gl071349

Saha, K. (2009). *Tropical circulation systems and monsoons*. Springer Science & Business Media.

Sandwell, D. T., Harper, H., Tozer, B., & Smith, W. H. (2019). Gravity field recovery from geodetic altimeter missions. *Advances in Space Research*, *68*(2), 1059–1072. https://doi.org/10.1016/j.asr.2019.09.011

Sandwell, D. T., & Smith, W. H. (2014). Slope correction for ocean radar altimetry. *Journal of Geodes*y, *88*(8), 765–771. https://doi.org/10.1007/s00190-014-0720-1

Sasaki, H., Klein, P., Qiu, B., & Sasai, Y. (2014). Impact of oceanic-scale interactions on the seasonal modulation of ocean dynamics by the atmosphere. *Nature Communications*, *5*(1), 1–8. https://doi.org/10.1038/ncomms6636

Sasaki, H., Klein, P., Sasai, Y., & Qiu, B. (2017). Regionality and seasonality of submesoscale and mesoscale turbulence in the North Pacific Ocean. *Ocean Dynamics*, *67*(9), 1195–1216. https://doi.org/10.1007/s10236-017-1083-y

Stommel, H. (1948). The westward intensification of wind-driven ocean currents. *Eos, Transactions American Geophysical Union*, *29*(2), 202–206. https://doi.org/10.1029/tr029i002p00202

Torres, H. S., Klein, P., Menemenlis, D., Qiu, B., Su, Z., Wang, J., et al. (2018). Partitioning ocean motions into balanced motions and internal gravity waves: A modeling study in anticipation of future space missions. *Journal of Geophysical Research: Oceans*, *123*(11), 8084–8105. https://doi.org/10.1029/2018jc014438

Uchida, T., Abernathey, R., & Smith, S. (2017). Seasonality of eddy kinetic energy in an eddy permitting global climate model. *Ocean Modelling*, *118*, 41–58. https://doi.org/10.1016/j.ocemod.2017.08.006

Vergara, O., Morrow, R., Pujol, I., Dibarboure, G., & Ubelmann, C. (2019). Revised global wave number spectra from recent altimeter observations. *Journal of Geophysical Research: Oceans*, *124*(6), 3523–3537. https://doi.org/10.1029/2018jc014844

Wessel, P., Smith, W. H., Scharroo, R., Luis, J., & Wobbe, F. (2013). Generic mapping tools: Improved version released. *Eos, Transactions American Geophysical Union*, *94*(45), 409–410. https://doi.org/10.1002/2013eo450001

Xu, Y., & Fu, L.-L. (2012). The effects of altimeter instrument noise on the estimation of the wavenumber spectrum of sea surface height. *Journal of Physical Oceanography*, *42*(12), 2229–2233. https://doi.org/10.1175/JPO-D-12-0106.1

Yu, Y., Gille, S. T., Sandwell, D. T., & McAuley, J. (2022). Global mesoscale ocean variability from multiyear altimetry: An analysis of the influencing factors. *Artificial Intelligence for the Earth Systems*, *1*(3), e210008. https://doi.org/10.1175/aies-d-21-0008.1

Zhang, S., Andersen, O. B., Kong, X., & Li, H. (2020). Inversion and validation of improved marine gravity field recovery in South China Sea by incorporating HY-2A altimeter waveform data. *Remote Sensing*, *12*(5), 802. https://doi.org/10.3390/rs12050802

Zhang, S., Li, J., Jin, T., & Che, D. (2018). Assessment of radar altimetry correction slopes for marine gravity recovery: A case study of Jason-1 GM data. *Journal of Applied Geophysics*, *151*, 90–102. https://doi.org/10.1016/j.jappgeo.2018.02.003

Zhang, S., & Sandwell, D. T. (2017). Retracking of SARAL/AltiKa radar altimetry waveforms for optimal gravity field recovery. *Marine Geodesy*, *40*(1), 40–56. https://doi.org/10.1080/01490419.2016.1265032

Zhang, S., Sandwell, D. T., Jin, T., & Li, D. (2017). Inversion of marine gravity anomalies over southeastern China seas from multi-satellite altimeter vertical deflections. *Journal of Applied Geophysics*, *137*, 128–137. https://doi.org/10.1016/j.jappgeo.2016.12.014